# X-ray crystal structure and anion selectivity features of the *E. Coli* Fluoride (Fluc) channel

by

Michal Tomasz Ruprecht

A thesis submitted in partial fulfillment of the Degree of Bachelor of Science in Neuroscience with Honors

University of Michigan

April 1, 2022

Committee:

Assistant Professor Randy Stockbridge, Chair

Professor Haoxing Xu

Assistant Professor Daniel Leventhal

Michal Tomasz Ruprecht
mrup@umich.edu
ORCID iD: 0000-0002-2787-1119

# Abstract

Fluoride anions ($F^-$) are ubiquitous in the environment. Accumulation of $F^-$ in microbial cells, especially at high concentrations, can lead to the inhibition of various enzymes necessary for metabolic processes. Fluoride ion exporter channels, or Flucs, are used by microorganisms to maintain $F^-$ levels below inhibitory concentrations. Two important features of Fluc channels differentiate them from other ion channels: Fluc channels are unusually specific for $F^-$ over chloride, and their dual-topology dimeric architecture, which is formed by the assembly of two polypeptides in an antiparallel transmembrane orientation, is unique. Both features are examined in this thesis. First, the X-ray crystal structure of the *Escherichia coli* strain of the channel was solved. Conserved residues and sequences important to the structure of the channel are discussed. Second, anion selectivity assays were conducted to determine why Fluc channels are highly specific for $F^-$ ions. Although initial experiments suggested that multiple anions are permeable, subsequent assays indicated that the permeability of these anions is sodium ion-dependent.

# Table of Contents

## Scientific Acknowledgements

I would like to express sincere appreciation to Prof. Randy Stockbridge for her assistance in the preparation of this manuscript. Thank you for welcoming me to the lab, providing me with an engaging environment even during a pandemic, challenging me to think critically about science, and sharing your passion for biology with me. In addition, I would like to thank the members of the Stockbridge Lab whose expertise was helpful during my work. Thank you, Dr. Ali Kermani, Dr. Benjamin McIlwain, Dr. Jason Devlin, Dr. Achala Chittor, Dr. Chris Macdonald, Olive Burata, Rachael Lucero, Chia-Yu "Winnie" Kang, Trevor Yeh, Fox Baudelaire, Ben Koff, Alain Sullivan, Alex Davis, and Kemal Demirer. Thank you also to the members of the committee, Drs. Haoxing Xu and Daniel Leventhal, for their valuable input.

The experiments presented in this thesis resulted from a close collaboration with Benjamin McIlwain, a postdoctoral fellow in our lab, who has permitted me to analyze crystallography data that he collected for this thesis. Data in **Table 2** that was collected by Dr. McIlwain is marked.

The introduction of this thesis was included in a publication I co-authored with Prof. Stockbridge and Dr. McIlwain (McIlwain, Ruprecht, et al., 2021). The introduction presented in this thesis was written by me with guidance from Prof. Stockbridge and Dr. McIlwain. Please note that my copyright transfer agreement with the publisher allows me to reuse the material in my publication.

## Personal Acknowledgements

I would like to express sincere appreciation to my mom, dad, sister, grandparents, and aunts for their never-ending love and support. I would also like to thank my friends, professors, teachers, and mentors.

## Extenuating Circumstances

I joined the Randy Stockbridge Lab during the winter 2020 semester, shortly before the COVID-19 pandemic began to affect the state of Michigan. When our lab pivoted to remote work, I co-wrote a publication on fluoride toxicity and membrane transport with Drs. Stockbridge and McIlwain (McIlwain, Ruprecht, et al., 2021).

During the fall 2020 semester, I continued to work remotely and focused on structurally characterizing the Fluc channel. I used crystallization data collected by Dr. McIlwain to solve the crystal structure of a Fluc channel homolog.

When the COVID-19 vaccine became readily available, I returned to in-person work during the summer and fall of 2021 and identified selectivity features of a Fluc channel homolog. Although I am disappointed that my in-person research experience was paused during the pandemic, I am proud of the work I have done and look forward to continuing my scientific endeavors in medical school.

# Introduction

## Environmental fluoride and weak acid accumulation

Fluorine is the most electronegative and reactive element in the periodic table, making it unstable in its uncharged state and hard to find in nature. Therefore, it easily acquires a negative charge and exists as an inorganic or organic fluoride compound. Fluoride anions ($F^-$) are ubiquitous in the environment. They're found in minerals, rocks, soil, and volcanoes (Weinstein & Davison, 2004). $F^-$ is also one of the most common anions in groundwater, which is usually contaminated by $F^-$-rich rocks (Jagtap et al., 2012).

When in acidic environments, $F^-$ becomes protonated to form hydrogen fluoride (HF), which is a weak acid with a $pK_a$ of 3.4. Fluoride transport across biological membranes occurs in the protonated form. Findings based on artificial lipid bilayers and pH electrodes show HF has a similar permeability coefficient to water (Barbier et al., 2010). Membrane-permeable HF in the environment (~5.5 pH) diffuses into the cytoplasm (~7 pH) under acidic conditions where it then dissociates into $F^-$ at neutral pH, leading to an accumulation of $F^-$. This phenomenon is called the weak acid accumulation effect. A one-to-one relationship is seen in the weak acid accumulation effect (**Equation 1**). To combat this effect, microorganisms use $F^-$ exporters to maintain levels below inhibitory concentrations (Ji et al., 2014), which will be further discussed.

$$\frac{[F^-]_{in}}{[F^-]_{out}} = \frac{[\mathrm{H}^+]_{out}}{[\mathrm{H}^+]_{in}}$$

**Equation 1:** Representation of ion movement during the weak acid accumulation effect.

$F^-$ prevalence, especially at high concentrations, endangers prokaryotic organisms. $F^-$ is usually present in the 10-100 μM range and poses a threat to bacteria by inhibiting (Ki=100 μM) enolase and pyrophosphatase enzymes important for glycolytic metabolism and nucleic acid synthesis (Adamek et al., 2005; R. Breaker, 2012). $F^-$ inhibits enzymes through cationic complexes with calcium ($Ca^{2+}$), magnesium ($Mg^{2+}$), and aluminum ($Al^{3+}$) cations (Barbier et al., 2010).

Enolase (2−phospho−D−glycerate hydrolase, EC 4.2.1.11) is a metalloenzyme that catalyzes the conversion of 2−phospho−D−glycerate (2-PGA) to phosphoenolpyruvate (PEP) in

the glycolysis pathway. $Ca^{2+}$ inhibits enolase activity by substituting catalytic $Mg^{2+}$ ions without blocking the substrate-binding site (Lebioda et al., 1991). $F^-$ then competes with the substrate 2-phosphoglycerate (2-PG) via a quaternary complex yeast enolase-$Mg^{2+}$-$F^-$-phosphate ion at the active site, causing a closed conformation and inhibiting 2-PG binding (Lebioda et al., 1993).

The other enzyme that is inhibited by $F^-$, pyrophosphatase (EC 3.6.1.1), catalyzes the conversion of one pyrophosphate ion to two phosphate ions in nucleic acid synthesis. The reaction takes place with four $Mg^{2+}$ ions, which help anchor the substrate to the active site. $F^-$ complexes with $Al^{3+}$ or beryllium ($Be^{2+}$) to mimic a phosphate and serve as a transition state mimic to inhibit catalysis of phosphoryl transfer reactions (Barbier et al., 2010; Li, 2003).

**Biological response to fluoride**

Due to the broad-spectrum sensitivity of metabolic processes to inhibition by $F^-$, microbes have mechanisms to mitigate the threat of $F^-$. However, the existence of the microbial mechanisms to reduce $F^-$ was unknown until 2012, when Ronald Breaker showed that the conserved *crcB* riboswitch motif, present in all domains of life, acts as a transcriptional "on-switch" upon $F^-$ binding (R. R. Breaker, 2012). When the motif is knocked out, $F^-$ sensitivity increases by 200-fold in an *Escherichia coli* strain, compared to the WT strain. This is mainly because of the lack of $F^-$ exporters when *crcB* is knocked out. Under the addition of NaF, highly conserved nucleotides in a 78-nucleotide RNA that encompasses the *crcB* motif, 78 Psy, undergo structural change to form a ligand-binding aptamer for $F^-$ with a dissociation constant (KD) of ~60 μM in *Pseudomonas syringae* (Baker et al., 2012).

$F^-$-sensitive metalloenzymes like enolase and the ATP-consuming DNA repair enzyme MutS are genes commonly associated with bacterial $F^-$ riboswitches. In addition, Na+/H+ antiporter genes frequently co-occur with $F^-$ riboswitches because they help maintain pH homeostasis, alleviating proton accumulation that occurs due to the weak acid accumulation effect. But the most common genes, present in almost half of all $F^-$-riboswitch controlled operons, code for membrane proteins responsible for $F^-$ export, the $CLC^F$ (CLC-Fluoride) and Fluc (Fluoride channel) proteins.

It's particularly interesting that RNA, as a negatively charged polyphosphate, can bind negatively charged anions like $F^-$. This is accomplished through coordination with $Mg^{2+}$ ions. $F^-$ is anchored by three $Mg^{2+}$ ions, which are octahedrally coordinated to water molecules and five

inward-pointing backbone phosphates, with three of the phosphates involved in bidentate coordination and two others in the monodentate coordination (Ren et al., 2012). This coordination positions $F^-$ into the negatively charged *crcB* pocket. The pocket is formed by two helical stems connected by a large asymmetric internal loop, which contains an overhang at the 5'-end able to participate in pseudoknot stabilizing interactions (Baker et al., 2012).

**$CLC^F$ $F^-/H^+$ antiporters**

Before $F^-$ riboswitches and associated genes were discovered, the CLC ($\underline{Cl}^-$ $\underline{c}$hannel) family of anion transport proteins was already well-known. Although $CLC^F$s belong to the CLC superfamily, strictly in the bacterial clade, the chloride ion ($Cl^-$)-transporting CLC (CLC-ecl) and $CLC^F$ (CLC-eca) are only ~20% identical and ~40% similar. $CLC^F$ shares some structural similarities with its CLC superfamily. The side-chain hydroxyl groups of highly conserved serine and tyrosine residues, as well as the glutamate ($Glu_{ex}$), are the mechanistic center of $Cl^-$ transport (Feng et al., 2012; Miller & Nguitragool, 2009). $CLC^F$s retain the conserved $Glu_{ex}$.

But $CLC^F$ differs from most $Cl^-$-transporting CLCs by sequence, function, and mechanism. One main sequential difference is the substitution of a conserved serine residue, contributing to $Cl^-$ selectivity, for a methionine or an asparagine residue, contributing to $F^-$ selectivity (Brammer et al., 2014; Last et al., 2018; Picollo et al., 2009). This sequential difference marks a phylogenetic split in the family that is followed by another sequential difference in the transporter-like glutamate, which has been thought to distinguish CLC channels from transporters. Instead, the methionine-containing subclade bears a channel-like valine (M-V subclade), while the asparagine-containing subclade bears a threonine (N-T subclade) (Brammer et al., 2014; Stockbridge et al., 2012). Third, the 1:1 $F^-/H^+$ stoichiometry of $CLC^F$ compared to the usual 2:1 stoichiometry of $Cl^-$ CLC channels is another main difference (Last et al., 2018). Because multiple $F^-$-coordinating moieties are similar to those of $Cl^-$ CLCs, it's important to distinguish the $F^-$ specificity in $CLC^F$. $CLC^F$ coordination of $F^-$ involves backbone amides, similar to other CLCs (Last et al., 2018).

Fluoride/proton antiporters in the riboswitch-controlled $CLC^F$ family combat $F^-$ accumulation in the cytoplasm. $CLC^F$ is present in soil and marine bacteria, plant and human pathogens, and gram-negative and gram-positive organisms (Stockbridge et al., 2012). Like other CLC proteins, $CLC^F$s assemble as homodimers. Each monomer contains 14 transmembrane $\alpha$-

helices comprised of two homologous seven-helix domains that are related to each other by internal inverted symmetry (Last & Miller, 2015; Last et al., 2018). Per their role in anion transport, the $\alpha$-helices are titled with respect to the membrane, defining electropositive internal and external aqueous vestibules that are 6-8Å deep. Breaks in these helices position the positive dipoles of the N-terminal ends of the helices near the central dehydrated anion-binding region of the protein and provide backbone amides to coordinate the transient anions.

**Fluc $F^-$ channels**

The second family of membrane proteins associated with the $F^-$ riboswitch is entirely dedicated to $F^-$ transport. Genes encoding these proteins, originally called *crcB*, are found not only in bacteria, but also in archaea, unicellular eukaryotes, fungi, plants, and filter-feeding ocean animals like sponges and sea anemones. The proteins encoded by the *crcB* genes are electrodiffusive $F^-$ channels. Electrodiffusion is the passive flow of $F^-$ down its electrochemical gradient. The channels were renamed Fluc (Fluoride channel) in bacteria and FEX (Fluoride exporter) in eukaryotes (McIlwain et al., 2018; Smith et al., 2015; Stockbridge et al., 2014; Stockbridge et al., 2013; Turman et al., 2015; Turman & Stockbridge, 2017).

The Fluc gene is found downstream of the *crcB* motif, and the protein consists of 120-130 amino acids (Li et al., 2013). Fluc channels conduct $10^7$ $F^-$ ions/second at −200 mV, independent of voltage (Stockbridge et al., 2013). Two important features of Fluc channels differentiate them from other ion channels. First, Fluc channels are unusually specific for $F^-$ over $Cl^-$ and second, they exhibit a dual-topology dimeric architecture, which is formed by the assembly of two polypeptides in an antiparallel transmembrane orientation (Stockbridge et al., 2014; Stockbridge et al., 2013).

Their specificity for $F^-$ over $Cl^-$ is over $10^4$-fold and allows a bacterium or yeast to express a constitutively open $F^-$ channel in its energy-coupling membrane while preventing a large export of $Cl^-$, which could collapse a cell's membrane potential (Stockbridge et al., 2013). In fact, when $F^-$ and $Cl^-$ are allowed to move down the electrochemical gradient into the cell, $F^-$ efflux occurs rapidly while $Cl^-$ efflux is undetectable (Stockbridge et al., 2013).

Through their antiparallel transmembrane assemblage, Fluc channels act as dimers of small polypeptides, which contain four transmembrane (TM) alpha-helices each (Stockbridge et al., 2014). This dual-topology assembly wasn't previously seen in ion channels but was known in

multidrug transporters in the small multidrug resistance (SMR) protein family such as EmrE (Stockbridge et al., 2013). Membrane transport proteins also assemble in a similar motif, with an inverted structural repeat in a single polypeptide chain (Forrest et al., 2011). This finding suggests many transporters independently evolved from this antiparallel architecture.

Fluc channels transport $F^-$ through a thermodynamically passive transmembrane channel via two methods. First, electric forces expel the anions out of the cytoplasm due to a negative membrane potential maintained by many classes of metabolizing cells. Or second, a large amount of extracellular HF is present because of the weak-acid accumulation effect, which is undermined by a Fluc channel (Stockbridge et al., 2013).

While Fluc channels are expressed in plants, fungi, and primitive marine animals, but not in mammals, this thesis will focus on homologs from *E. coli* (Ec2) and *Bordetella pertussis* (Bpe). Bacterial Fluc channels assemble as dimers of small subunits and are composed of 120-130 residues with four TM helix motifs, short N- and C-termini, and a strictly conserved sequence in TM3 (TGXXXGLTTFSTFXXXE, with X denoting any amino acid) (Stockbridge et al., 2013). The dimer interface is within the membrane and TM3 is split into TM3a and TM3b by a non-helical segment (Stockbridge et al., 2015). The channel is shaped like an hourglass and characterized by its wide vestibules that symmetrically open to two aqueous solutions separated by a plug of protein 10-15Å thick (Stockbridge et al., 2015). A highly conserved TM1 arginine residue (Arg23 in Bpe) protrudes into each vestibule, suggesting an electrostatic lure for $F^-$ (Stockbridge et al., 2015).

Recent crystal structures reveal two active fluoride pores (Stockbridge et al., 2014). The two $F^-$ ions, separated by 12Å, are present in each ion-permeation pathway (Last et al., 2017). Both pathways are mostly narrow and anhydrous, with side chains filling up space (Stockbridge et al., 2015). The lower $F^-$ approaches the wide aqueous vestibules on the two ends of the channel, while the other $F^-$ is found buried deep in the protein (Last et al., 2017). The two $F^-$ ions are positioned in a vertical line slightly off normal to the membrane plane, creating a narrow permeation pathway (Last et al., 2016; Stockbridge et al., 2015). The orientation of the two $F^-$ ions suggests a double-barreled, two-pore structure in Bpe and Ec2. Furthermore, McIlwain and colleagues found that the crystal structures of Fluc represent the functional, $F^-$-conducting conformation of the channel (McIlwain et al., 2018).

Four electron densities, which were later established as $F^-$ ions, are located in the crevices between TM2, TM3b, and TM4 near the edge of the channel, far from the vestibules and central plug (Stockbridge et al., 2015). These crevices are formed by a protrusion from the TM1-TM2 and TM3b-TM4 connecting loops of the channel (Stockbridge et al., 2015). These densities are surrounded by electropositive side chains, which engage in strong hydrogen bond-accepting interactions with $F^-$ (Stockbridge et al., 2015). Several conserved groups are notable, including an asparagine (Asn43 in Bpe, Asn41 in Ec2) in TM2 and two serines (Ser108 and Ser112 in Bpe) in TM4 (Stockbridge et al., 2015). The two serines facing the pore in TM4 are different hydrogen bond donors of low sequence identity, with every fourth residue in TM4 varying between asparagine, serine, threonine, histidine, or tyrosine. This suggests a polar track is needed for recognition of $F^-$ (Last et al., 2016; Stockbridge et al., 2015).

In addition, conserved polar residues are formed from two pairs of highly conserved aromatic phenylalanines (Phe82 and Phe85 in Bpe) in TM3, on a side-on electropositive orientation into the pore (Stockbridge et al., 2015). Last and colleagues confirmed these findings, concluding that the Phe82 and Phe85 sites most likely act as functionally relevant $F^-$ binding sites (Last et al., 2016). Furthermore, resonance in phenylalanine from its phenyl ring creates a positively charged hydrogen, which would be effective in strong hydrogen bonding with $F^-$. Phe80 and Phe83, the equivalents to Phe82 and Phe85, in Ec2 are both located in TM3b, however, one Phe80 and Phe83 pair is located in pore I and another is located in pore II (Last et al., 2016). Because of this architecture, each Fluc monomer contributes a phenylalanine to each pore (Last et al., 2016). The two phenylalanines are vital to the function of Fluc channels. Mutations to the phenylalanines inhibited the channel and prevented $F^-$ binding (Last et al., 2016).

The two-pore structure demonstrates evolutionary drift in eukaryotic Fluc channels, with inverted repeats of the two homologous Fluc domains fused into a single polypeptide. Pore II retains the highly conserved sequence that arises from the carboxy-terminal domain, which is typical of homodimeric bacterial Flucs (Stockbridge et al., 2015). By contrast, the same residues in pore I are less conserved and mostly arise from the amino-terminal domain, which is prevalent along the TM4 polar track (Stockbridge et al., 2015). A similar pattern is seen in the conserved phenylalanines, suggesting that pore II alone participates in $F^-$ export in eukaryotic Flucs.

A fifth electron density, far removed from the $F^-$ permeation pathway, is also present and has been identified as a sodium cation ($Na^+$). The ligand is tetrahedrally complexed by four carbonyl oxygens, suggesting the ligand is cationic. Charge, chemical considerations of the coordination sphere, and the presence of $Na^+$ in purification buffers and crystallization solutions indicated that the density is $Na^+$ (McIlwain et al., 2020; Stockbridge et al., 2015). $Na^+$ binds at a site formed by the cross of the two TM3 helices via a pair of equivalent amino acids (Gly77 and Thr80 in Bpe) at the center of the membrane, along the two-fold symmetry axis (Stockbridge et al., 2015). The binding site is also highly selective for $Na^+$ over other cations like $K^+$ and $Mg^{2+}$ and has proved to be essential for proper Fluc conducting conformation (McIlwain et al., 2020). Furthermore, the electropositive nature of $Na^+$ allows for electrostatic stabilization in the presence of $F^-$ (McIlwain et al., 2020). This architecture proves to be unique and the first example of $Na^+$ as a strictly structural element and not a transported substrate (McIlwain et al., 2020).

Fluc channels are filled with side chains that are negotiated by fast ion translocation rates (~ $10^6$ ions/sec), unlike traditional channels with aqueous tunnels that are lined with polar groups (Stockbridge et al., 2015). This unique architecture calls for the proposed "channsporter" mechanism, which consists of coordinated protein movement involved in $F^-$ export (Stockbridge et al., 2015). During permeation, Asn43 in Bpe experiences a rotameric switch such that the amide nitrogen remains hydrogen-bonded, while the anion moves along the pore (Stockbridge et al., 2015).

**Thesis goals**

It is known that changes in membrane potential can be propagated to neighboring bacteria, changing their behavior (Humphries et al., 2017). To gain a better understanding of this mechanism, I studied a membrane protein in bacteria, Fluc, that transports the charged substrate $F^-$. Prior research has identified the structure and selectivity features of certain Fluc channel homologs; however, it is unknown if Fluc channels evolved the ability to export ions other than $F^-$. Because Fluc channels are so selective for $F^-$, they are good model systems for understanding anion selectivity by ion channels.

My first aim was to understand the structure of the Fluc-Ec2 homolog. I analyzed crystallography data collected by Dr. McIlwain and solved the crystal structure of Ec2. After solving the structure, I analyzed important residues in the channel.

My second aim was to determine if the Ec2 homolog transports anions with a $pK_a$ similar to $F^-$. I chose to study four potassium and sodium salts, including chloride, cyanate, chlorate, and bromate. I hypothesized that the Ec2 homolog evolved the ability to transport anions other than $F^-$. I conducted electrophysiology experiments to understand how Fluc channels distinguish between $F^-$ and other anions.

# Materials and Methods

## Sequence alignment of protein homologs

Homologous Fluc channel protein sequences from 14 clinically relevant bacteria were collected from the Basic Local Alignment Search Tool (BLAST) (Altschul et al., 1990). Sequence alignment was conducted with Seaview (Gouy et al., 2010).

## Protein expression, purification, and reconstitution

Protein expression, purification, and reconstruction were conducted by Dr. McIlwain and the following procedure is adapted from McIlwain, Gundepudi, et al. (2021). "Fluc-Ec2 channels were constructed using standard molecular biology techniques and sequence verification. Based on protocols in previous studies, histidine-tagged Fluc-Ec2 was expressed in *E. coli* and purified by cobalt affinity chromatography (McIlwain et al., 2020; Stockbridge et al., 2014; Stockbridge et al., 2015). The buffer for the final size-exclusion step was 100 mM NaBr, 10 mM 2-[4-(2-hydroxyethyl)piperazin-1-yl]ethanesulfonic acid (HEPES), pH 7, for crystallography applications, or 100 mM NaCl, 10 mM HEPES, pH 7, for functional reconstitution. For reconstitution, proteins were mixed with detergent-solubilized *E. coli* polar lipids (Avanti Polar Lipids; 10 mg/ml) at a ratio of 5 μg protein/mg lipid for macroscopic bilayer experiments. The protein/detergent/lipid mixture was dialyzed for 36 hr (6 L buffer per 50 mg lipid over three buffer changes). Proteoliposomes were stored at −80°C until use, at which point the suspension was freeze-thawed three times and extruded 21 times through a 400 nm filter to form liposomes."

## X-ray crystallography

X-ray crystallography data was collected by Dr. McIlwain and the following procedure is adapted from McIlwain, Gundepudi, et al. (2021). "After purification, monobody S9 and Fluc-Ec2 were mixed in a 1:1 molar ratio according to published protocols (Stockbridge et al., 2015). Crystals were formed in either 0.1 M glycine, pH 8.7–9.2, 31–36% polyethylene glycol (PEG) 600 or 0.1 M ammonium sulfate, 0.1 M N-(2-acetamido)iminoacetate (ADA), pH 6–6.5, 31–36% PEG 600 over 3–7 days and were frozen in liquid nitrogen before data collection at 13.5 keV at the Life Sciences Collaborative Access Team beamline 21-ID-D at the Advanced Photon Source, Argonne National Laboratory."

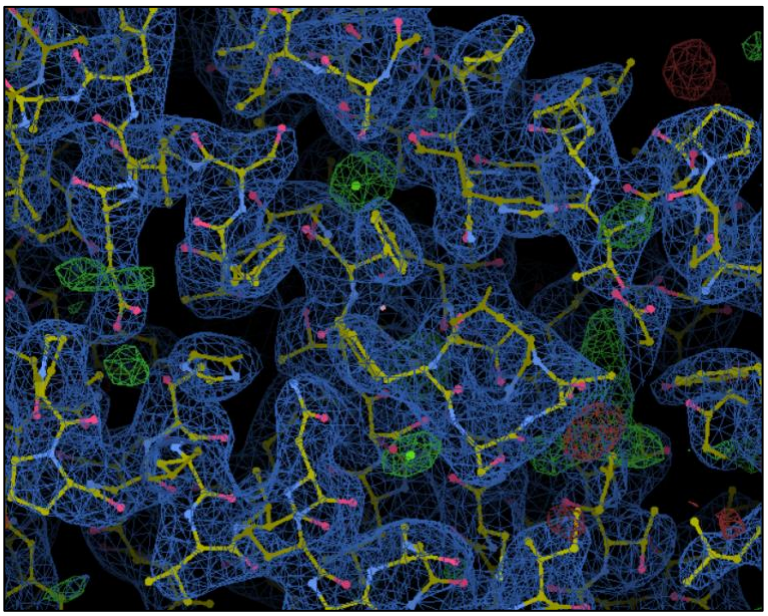

**Figure 1:** Residues were fit into the electron density through adjustments to the rotamers, which are different conformational isomers with varying bond angles. Both alanine and glycine do not have rotamers. Revisions were conducted using real-space refinement.

I solved the structure of the Fluc-Ec2 homolog using diffraction data collected by Dr. McIlwain. CCP4i was used to run a molecular replacement and generate an anomalous map and H-bond restraints (Potterton et al., 2003; Winn et al., 2011). The following procedure is adapted from McIlwain, Gundepudi, et al. (2021). "Phases were calculated by molecular replacement with Phaser (McCoy et al., 2007) using Fluc-Ec2 and the monobody S9 as search models (pdb:5A43), followed by refinement with Refmac (Murshudov et al., 2011) and model building in real space with Coot (Emsley et al., 2010)." Coot was used to fit residues into the electron density, as shown in **Figure 1**, and mutate all selenomethionine residues to methionine. Analysis of the model was conducted with PyMOL (Schrodinger, 2010). Crystallography statistics from MolProbity, a structure-validation web service, were used to analyze the strength and validity of the proposed structure (Williams et al., 2018).

**Planar lipid bilayer electrophysiology**

I conducted planar lipid bilayer electrophysiology experiments using Fluc-Ec2 channels provided to me by Dr. McIlwain. Lipid bilayer electrophysiology was used to understand

current-voltage (I-V) relationships and the voltage-dependent mechanisms of Fluc-Ec2 through the manipulation of membrane potential, known as voltage clamp (Stockbridge & Tsai, 2015). In the experiments described below, a holding voltage of −200 mV was applied to one side of the bilayer, while a potential in the range of −200 mV to +200 mV was applied to the opposite side. The Axopatch 200B amplifier and pClamp 8 were used for the experiments below (Axon Instruments, Foster City, CA, U.S.A.). A setup of the experiment can be found in **Figure 2**. The following procedure is adapted from McIlwain, Gundepudi, et al. (2021) and Stockbridge et al. (2013). "Electrophysiological recordings were acquired at a holding voltage of −200 mV, electronically filtered at 1 kHz during acquisition, and digitally filtered to 500 Hz for analysis. Solutions in the cis and trans chambers varied as described in the text."

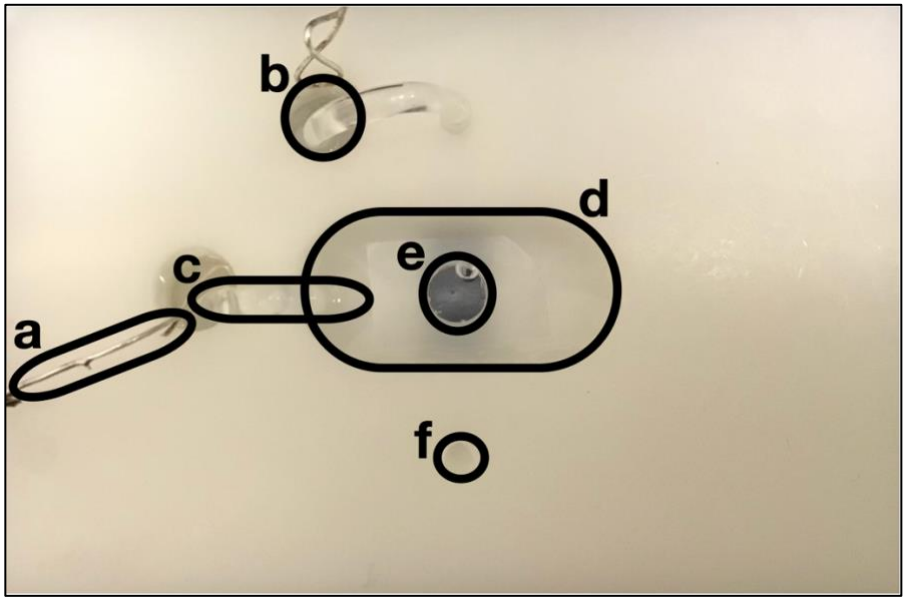


**Figure 2**: The planar lipid bilayer electrophysiology experiment set up. There is a duplicate component for some of the labeled elements (**a-c, f**) in the setup, but only one of the two is labeled. (**a-b**) Location of the following reaction: $Ag + Cl^- \leftrightarrow AgCl + e^-$. (**a**) The Ag probe provides an electrical connection between the solution and amplifier. (**b**) Vessel containing the salt bridge buffer, 300 mM KCl with 10 mM 3-(N-morpholino)propanesulfonic acid (MOPS), pH 7. (**c-d**) The salt bridge electrically connects the electrode with both chambers. (**c**) Agar salt bridge. (**d**) Cis chamber, containing 290 mM KF and 10 mM NaF with 10 mM HEPES, pH 7 during every experiment except for the bromate gradient experiment. (**e**) Trans chamber, containing 290 mM of the potassium and 10 mM of the sodium salt of each anion tested with 10

mM HEPES, pH 7 during every experiment except for the bromate gradient experiment. The trans chamber is separated from the cis chamber with a plastic partition, which contains a small hole. (**f**) Access port to the trans chamber.

McIlwain et al. (2020) found that a sodium ion is needed for proper Fluc conducting conformation and that the electropositive nature of the ion allows for electrostatic stabilization in the presence of $F^-$. To avoid interference between exogenous sodium and the channel, we initially avoided using sodium salts. However, we concluded that a small molar amount of sodium, approximately 10 mM, is needed to stabilize the channel. The following procedure is also adapted from McIlwain, Gundepudi, et al. (2021) and Stockbridge et al. (2013). "Typical solutions contained 290 mM KF and 10 mM NaF with 10 mM HEPES, pH 7. For anion selectivity experiments, sodium and potassium salts of $BrO_3^-$ (bromate), $Cl^-$ (chloride), $OCN^-$ (cyanate), and $ClO_3^-$ (chlorate) were tested because of the similarity of their $pK_a$s to the $pK_a$ of HF (3.4) and their ability to be hydrogen bond acceptors. The lone pairs on the oxygen atoms of bromate, cyanate, and chlorate make these anions excellent candidates as hydrogen bond acceptors. For these experiments, 290 mM of the potassium and 10 mM of the sodium salt of each anion (eg. 290 mM KCl and 10 mM NaCl) with 10 mM HEPES, pH 7 was prepared and added to the trans chamber. For the bromate gradient experiment, 20 mM $KBrO_3$ and 10 $NaBrO_3$ with 10 mM HEPES, pH 7 was prepared and added to the trans chamber. Macroscopic bilayer recordings shown are representative of two to three independent bilayer experiments for each experiment. All constructs used for electrophysiology experiments were purified from at least two independent protein preparations, and no prep-to-prep variation was observed." To understand anion selectivity in Fluc-Ec2, reversal potentials of each anion tested were calculated using Clampex (Axon Instruments). Graphs were created using GraphPad Prism (GraphPad Software Inc., San Diego, CA, U.S.A.). ChemDraw was used to visualize the chemical structures of each anion (CambridgeSoft, Cambridge, MA, U.S.A).

# Results

## Identification of conserved residues

Conserved amino acid residues can provide insight into regions of Fluc-Ec2 that are important to the protein's function. To identify conserved residues in Fluc-Ec2, a sequence alignment of Flucs from 14 clinically relevant bacteria, including *Brucella abortus*, *Bacillus anthracis*, and *Vibrio parahaemolyticus*, was created.

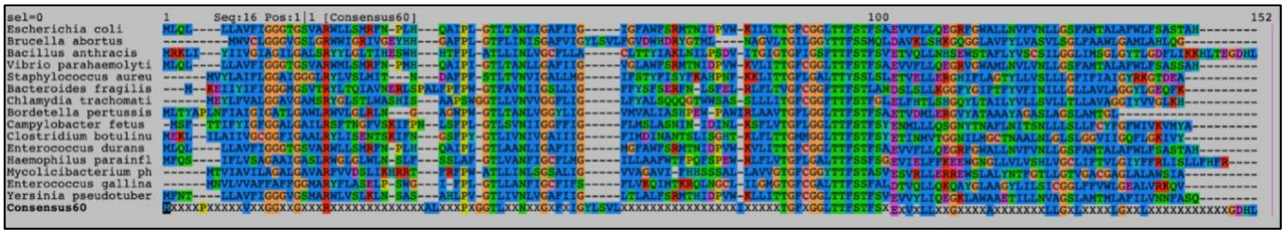


**Figure 3:** Sequence alignment of Fluc-Ec2 with 14 Fluc homologs.

It is interesting to observe that the Fluc channel sequence of every species is not the same length, as shown in **Figure 3**. For example, the *E. coli* sequence is 127 amino acids long, while the *B. abortus* sequence is 123 amino acids long. Residues that are conversed among all the sequences examined include Arg19, Asn41, and Gly44 (Fluc-Ec2 numbering). Previous studies have identified that the highly conserved Arg19 from TM1 protrudes into each vestibule and contributes to the electropositive environment (Macdonald & Stockbridge, 2017). This environment may act as an electrostatic lure for $F^-$. Another highly conserved residue, Asn41 in TM2, is involved in the coordination of $F^-$ ions (Macdonald & Stockbridge, 2017). This hydrogen bond donor has also been proposed to contribute to the polar track of the protein, which is characterized by its polarity and dehydrated stretch. In fact, when Asn41 is mutated, the channel typically loses its ability to transport $F^-$ (Stockbridge et al., 2015). Gly44 is also an interesting residue. Because of its small size and greater conformational mobility, it may be involved in supporting the dimeric structure.

The following residues and sequences are also conserved, but not by every sequence examined: GGXXG (11-15), Pro34, GTL (36-38), Gly49, and TGFXGGLTTFSTFSXE (71-86). As discussed above with the Gly44 residue, both GGXXG (11-15) and Gly49 may serve a similar role. In contrast, Pro34 may serve to restrict conformational mobility. Found in the

conserved sequence of GTL (36-38) is Thr37, which is in close 3D proximity to Glu86 (this residue is more thoroughly discussed below) and Asn102. They are proposed to associate together due to their proximity and high propensity to hydrogen bond. Due to the proximity of Asn102 to an $F^-$ ion within the pore, it is suggested that this residue also hydrogen bonds with the $F^-$ (McIlwain, Gundepudi, et al., 2021).

| | 71 | 72 | 73 | 74 | 75 | 76 | 77 | 78 | 79 | 80 | 81 | 82 | 83 | 84 | 85 | 86 |
|---|---|---|---|---|---|---|---|---|---|---|---|---|---|---|---|---|
| ***Escherichia coli*** | T | G | F | C | G | G | L | T | T | F | S | T | F | S | A | E |
| *Brucella abortus* | T | G | I | L | G | G | Y | T | T | F | S | S | M | Q | L | D |
| *Bacillus anthracis* | T | G | F | I | G | S | F | T | T | F | S | T | F | S | V | E |
| *Vibrio parahaemolyticus* | T | G | F | C | G | G | L | T | T | F | S | T | F | S | A | E |
| *Staphylococcus aureus* | T | G | F | L | G | A | L | T | T | Y | S | S | L | S | L | E |
| *Bacteroides fragilis* | V | G | F | C | G | G | F | T | T | F | S | T | L | A | N | D |
| *Chlamydia trachomatis* | T | G | F | C | G | G | F | T | T | F | S | T | F | G | L | E |
| *Bordetella pertussis* | T | G | F | L | G | G | L | T | T | F | S | T | F | S | A | E |
| *Campylobacter fetus* | T | G | F | L | G | G | L | T | T | F | S | T | F | S | Y | E |
| *Clostridium botulinum* | T | G | M | M | G | G | L | T | T | F | S | T | F | S | Y | E |
| *Enterococcus durans* | T | G | F | C | G | G | L | T | T | F | S | T | F | S | A | E |
| *Haemophilus parainfluenzae* | T | G | F | L | G | A | L | T | T | F | S | S | F | S | G | E |
| *Mycolicibacterium phlei* | T | G | F | C | G | G | Y | T | T | F | S | T | A | S | V | E |
| *Enterococcus gallinarum* | T | G | F | C | G | A | L | T | T | F | S | S | F | A | L | D |
| *Yersinia pseudotuberculosis* | T | G | F | C | G | G | L | T | T | F | S | T | F | S | V | E |

**Figure 4:** Sequence alignment of the TGFXGGLTTFSTFSXE region (71-86, Fluc-Ec2 numbering). Residues highlighted in green are conserved among all sequences, while orange residues are partially conserved.

Of note in the sequence of TGFXGGLTTFSTFSXE (71-86), shown in **Figure 4**, are Ser81 and Thr82 from the TM3 break. Ser81 is conserved in all the sequences examined and the hydroxyl groups of both residues have been proposed to be involved in the $F^-$ permeation pathway. In fact, when Ser81 is mutated to either cysteine or threonine, the channel loses its ability to transport $F^-$ ions (McIlwain, Gundepudi, et al., 2021). Phe80 and 83, also part of the conserved sequence, have been proposed to coordinate $F^-$ ions through their electropositive edges. When either residue is mutated to a nonpolarizable hydrophobic residue like isoleucine, $F^-$ transport is mostly or totally abolished (Stockbridge et al., 2015). Notably, when the

phenylalanines are mutated to a hydrophobic and polarizable residue like methionine, $F^-$ ion conductance is unchanged (Last et al., 2017). Glu86, which is also highly conserved in the sequence, has been proposed to add to anion selectivity. Although its role is unclear, McIlwain, Ruprecht, et al. (2021) have suggested that the residue may contribute to the dissociation of $F^-$ from the pore through its negative charge. Finally, Gly75 and Thr78, also found in the conserved sequence, have been found to be the binding site of $Na^+$. Both sequences are found at the cross of the two TM3 helices (Stockbridge et al., 2015).

**Analysis of the proposed structure**

Although Dr. McIlwain and colleagues solved the crystal structure of Ec2 (pdb:5A43), the goal of this thesis was to examine important structural features that affect the function of the protein. The structure used in this thesis was co-crystallized with bromide, a halide that anomalously scatters X-ray beams. Therefore, it is visible in electron density maps and used to unambiguously identify anion binding sites. Following the generation of the anomalous map, an anomalous signal was not observed in the dataset. The search models used were Fluc monomer and S9 monobody. The S9 monobody blocks $F^-$ permeation in this homolog, as shown in **Figure 5**. The protein was crystallized in the $P4_1$ space group, and the previous structure was used to determine phases using molecular replacement.

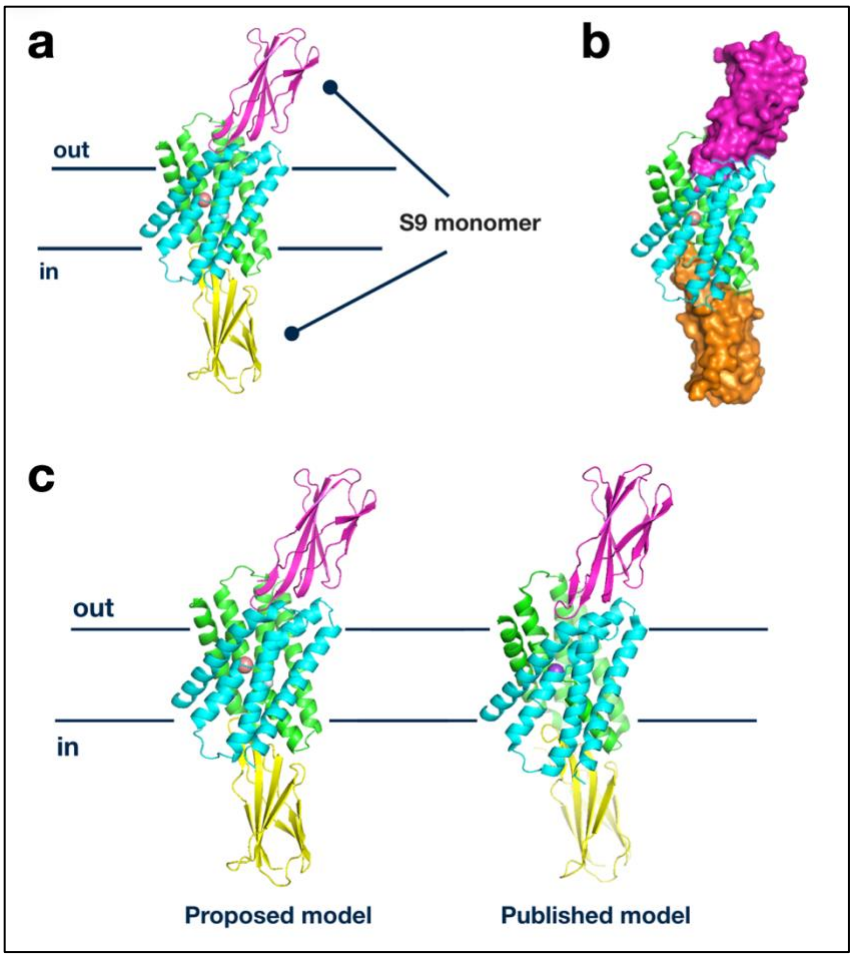


**Figure 5:** Proposed model of Fluc-Ec2. Horizontal lines denote the approximate membrane boundaries. (**a**) Cartoon representation. (**b**) Surface representation. (**c**) Comparison of the proposed model to the published model (pdb:5A43).

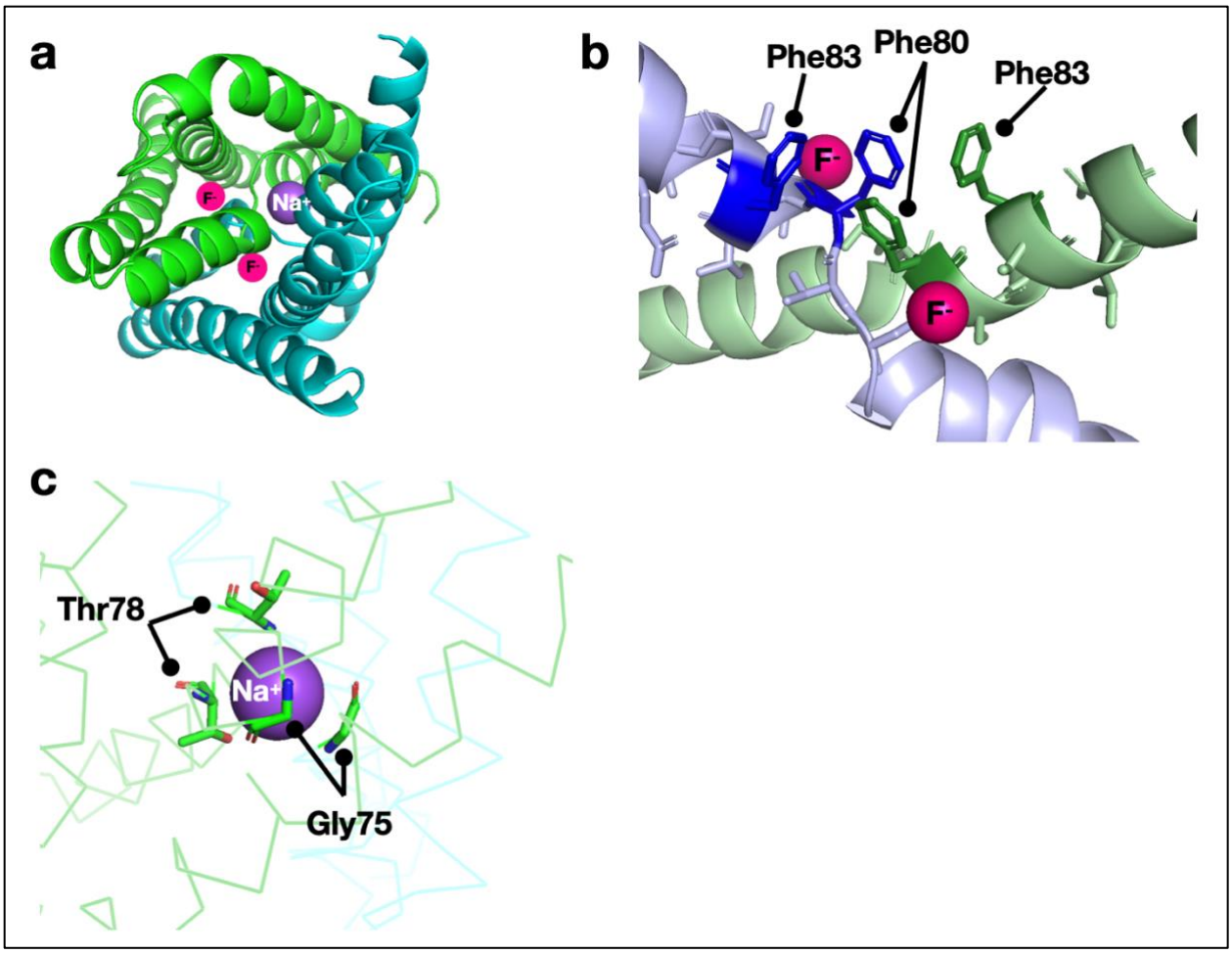


**Figure 6:** Binding sites of the $F^-$ and $Na^+$ ions. The pink spheres denote $F^-$ ions, while the purple spheres denote the $Na^+$ ion. (**a**) Cartoon representation from a top-down view showing the location of the $F^-$ and $Na^+$ ion binding sites. (**b**) Residues involved in the binding of $F^-$ are shown as sticks. (**c**) Residues involved in the binding of $Na^+$ are shown as sticks.

As mentioned in the section above, the highly conserved side chains Phe80 and 83 are involved in the coordination of $F^-$ ions. Due to resonance and pi orbitals of the phenylalanines, a slight positive charge off the side of the ring is present. This property allows edgewise interactions of phenylalanines like Phe80 and 83 with anions like $F^-$. These interactions are called anion-quadrupole interactions (McIlwain, Ruprecht, et al., 2021). As shown in **Figure 6**, the electropositive edge of each phenylalanine is adjacent to the electronegative face of the next phenylalanine. Through side-on coordination by the electropositive quadrupoles of the ring edges, the polarizable phenylalanines interact with the $F^-$ ions.

The binding site of the $Na^+$ ion, located at the cross of the two TM3 helices, is surrounded by partially negative carbonyl groups in sidechains Gly75 and Thr78, shown in **Figure 6**. These residues, located at the center of the membrane along the two-fold symmetry axis, coordinate $Na^+$ and are highly selective for the ion.

| | **102** | 103 | 104 | 105 | **106** | 107 | 108 | 109 | **110** |
|---|---|---|---|---|---|---|---|---|---|
| ***Escherichia coli*** (plasmid) | S | V | L | V | H | V | I | G | S |
| ***Escherichia coli*** (genomic) | N | V | F | V | N | L | L | G | S |
| *Brucella abortus** | Y | L | V | A | S | V | L | S | G |
| *Bacillus anthracis** | Y | V | S | C | S | I | L | G | G |
| *Vibrio parahaemolyticus* | N | V | L | V | N | L | L | G | S |
| *Staphylococcus aureus** | Y | L | L | V | S | L | L | L | G |
| *Bacteroides fragilis** | Y | V | F | I | N | I | L | L | G |
| *Chlamydia trachomatis* | Y | V | L | L | S | V | L | L | T |
| *Bordetella pertussis* | Y | A | G | A | S | L | A | G | S |
| *Campylobacter fetus* | N | I | T | S | N | L | L | L | S |
| *Clostridium botulinum* | N | A | A | L | N | L | G | L | S |
| *Enterococcus durans* | N | V | F | V | N | L | L | G | S |
| *Haemophilus parainfluenzae** | V | L | V | S | H | L | V | G | C |
| *Mycolicibacterium phlei* | N | T | F | G | T | L | L | G | T |
| *Enterococcus gallinarum** | Y | L | I | L | S | I | C | G | G |
| *Yersinia pseudotuberculosis* | T | I | L | L | N | V | A | G | S |

**Figure 7:** Sequence alignment of the TM4 polar track region (102-110, Fluc-Ec2 numbering). Residues highlighted in blue are polar, while residues highlighted in red are non-polar. Sequences with non-polar residue(s) in the polar track region are marked with an asterisk.

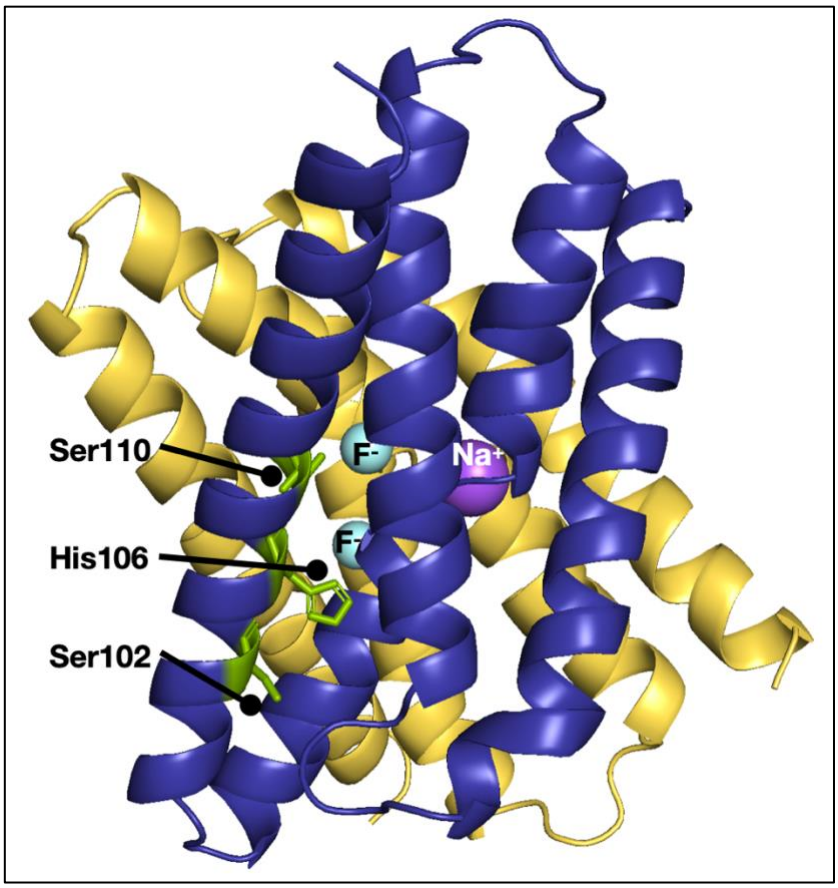


**Figure 8:** Side chains in the Fluc-Ec2 SXXXHXXXS (102-110) plasmid sequence that make up the polar track are shown as sticks. The cyan spheres denote $F^-$ ions, while the purple sphere denotes the $Na^+$ ion.

Another important structural feature of the Fluc channel is its polar track, which is involved in the $F^-$ permeation pathway. This region is characterized by a stretch of hydrogen bond donors at every fourth position, or one hydrogen bond donor per helical turn. Although the side chains are not conserved, the polar, hydrogen bond–donating characteristic is, as shown in **Figure 7**. In the *E. coli* genomic Fluc sequence, the region consists of NXXXNXXXS (102-110). In contrast, the plasmid Fluc-Ec2 sequence consists of SXXXHXXXS (102-110), as shown in **Figure 8**.

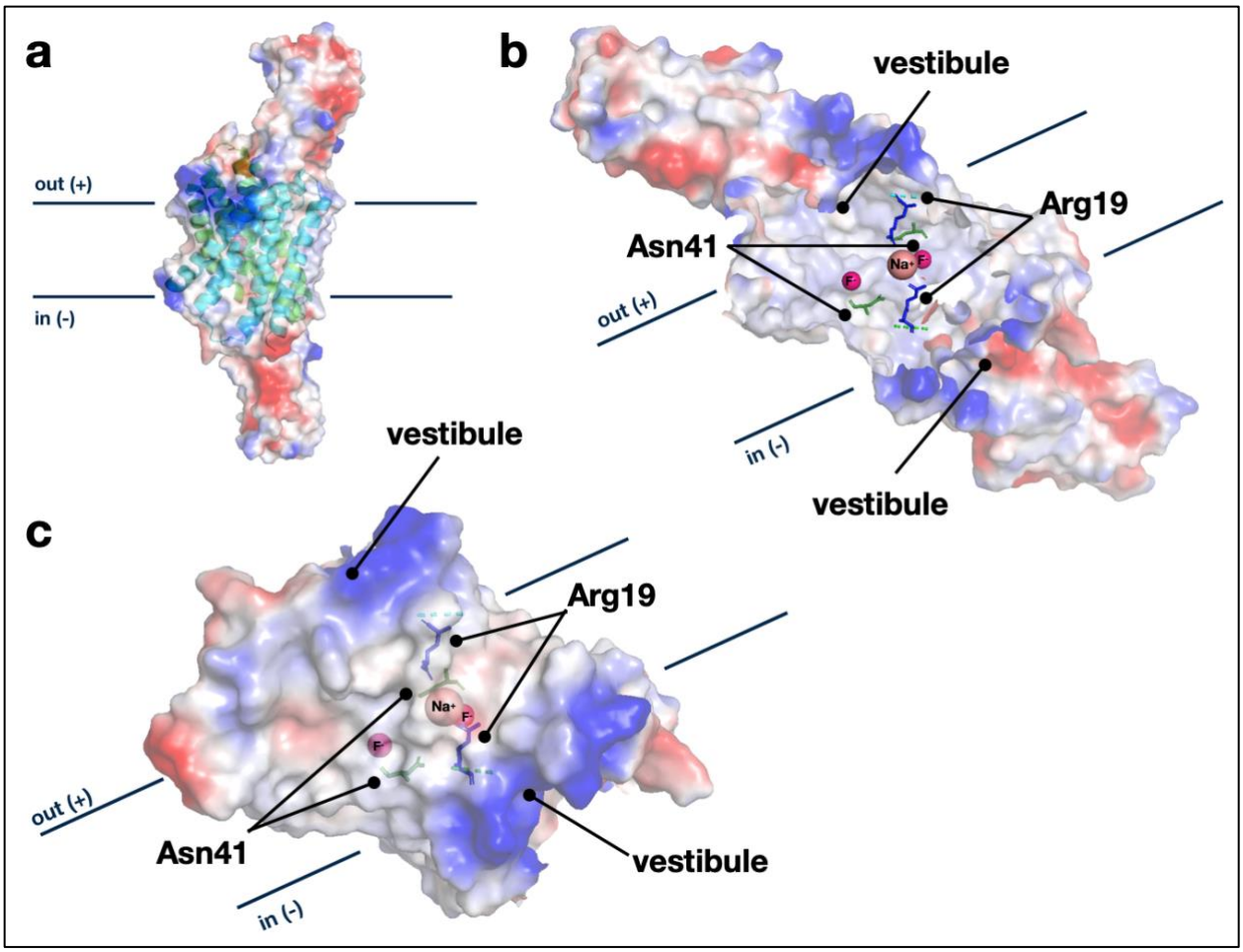


**Figure 9:** Electrostatic surfaces of Fluc-Ec2. The red hue denotes an electronegative surface, while the blue hue denotes an electropositive surface. Horizontal lines denote the approximate membrane boundaries with typical membrane polarization indicated with plus and minus symbols. (**b**-**c**) Highly conserved side chains Arg19 and Asn41 are shown as sticks. The pink spheres denote $F^-$ ions, while the brown spheres denote the $Na^+$ ion.

To gain a better understanding of the charges involved in the $F^-$ ion permeation pathway, an electrostatic surface rendering of the proposed structure was created, as shown in **Figure 9**. The symmetrical hourglass shape adopted by the channel includes two aqueous, electropositive vestibules on both sides of the membrane. The vestibules are separated by a 10Å thick protein plug, which houses the structural $Na^+$. The $Na^+$ and Arg19 side chain, shown in **Figure 9**, render both vestibules electropositive. Due to the electropositive nature of these vestibules, $F^-$ ions are proposed to accumulate in the vestibules. In fact, $F^-$ currents are inhibited if the vestibule is occluded by the bulky, negatively charged thiol-reactive reagent Sodium (2-

sulfonatoethyl)methanethiosulfonate (MTSES) (McIlwain, Gundepudi, et al., 2021). In addition to these features, the electropositive Arg19, located in the aqueous vestibule, most likely acts as an electrostatic barrier to $Na^+$ dissociation. The $Na^+$ ion is positioned about 5Å away from Arg19. In addition to this conserved residue, Asn41 is also a key player in the $F^-$ permeation pathway. In fact, it has been suggested that Asn41 may aid in the stabilization of the helical break that is located near the $Na^+$ binding site (McIlwain et al., 2020).

**Strength and validity of the proposed structure**

To validate the strength of the proposed structure, protein geometry, atom contacts, and other metrics were obtained, shown in **Table 1**. While the clashscore worsened after manual refinement, most other metrics improved. The increased clashscore may be a result of the corrections made to the backbone of the structure while fitting residues into the electron density. The same may be used to explain the increase in Ramachandran outliers. Due to a decrease in the number of poor rotamers and an increase in the amount of Ramachandran favored and favored rotamers, the proposed structure is improved. In fact, the MolProbity score, which is a value that summarizes model quality, including the clashscore and an analysis of the Ramachandran and rotamer statistics, improved by 9%.

Ramachandran plots of the model in **Figure 10** were used to examine Ψ and Φ dihedral angles, which provide insight into unfavorable geometry such as steric crowding. Though there is a very low number of Ramachandran outliers, the largest collection of Ramachandran outliers is in the general plot. These include Ser81, which is a highly conserved residue examined in **Figure 4**. Its involvement in the $F^-$ permeation pathway may result in slight strain.

**Table 1:** MolProbity statistics comparing the model before and after manual refinement[a]

| | **Before** | | **After** | |
|---|---|---|---|---|
| Clashscore (N=186, 2.71Å ± 0.25Å) | 10.81 | 98$^{th}$ percentile | 11.68 | 97$^{th}$ percentile |
| Poor rotamers | 31 | 8.16% | 25 | 6.58% |
| Favored rotamers | 309 | 81.32% | 318 | 83.68% |
| Ramachandran outliers | 7 | 1.61% | 8 | 1.83% |
| Ramachandran favored | 396 | 90.83% | 402 | 92.20% |
| Rama distribution Z-score | −3.96 ± 0.33 | | −4.05 ± 0.31 | |
| MolProbity score (N=5298, 2.71Å ± 0.25Å) | 2.77 | 72$^{nd}$ percentile | 2.68 | 77$^{th}$ percentile |
| Cβ deviations >0.25Å | 5 | 1.23% | 2 | 0.49% |
| Bad bonds | 0 / 3468 | 0.00% | 0 / 3468 | 0.00% |
| Bad angles | 18 / 4754 | 0.38% | 12 / 4754 | 0.25% |
| Cis Prolines | 2 / 24 | 8.33% | 2 / 24 | 8.33% |
| Chiral volume outliers | 0/590 | | 0/590 | |
| Waters with clashes | 0/0 | 0.00% | 0/0 | 0.00% |

[a] Values marked in green denote an improvement after manual refinement, while red values denote the opposite. Values without highlighting were unchanged after manual refinement.

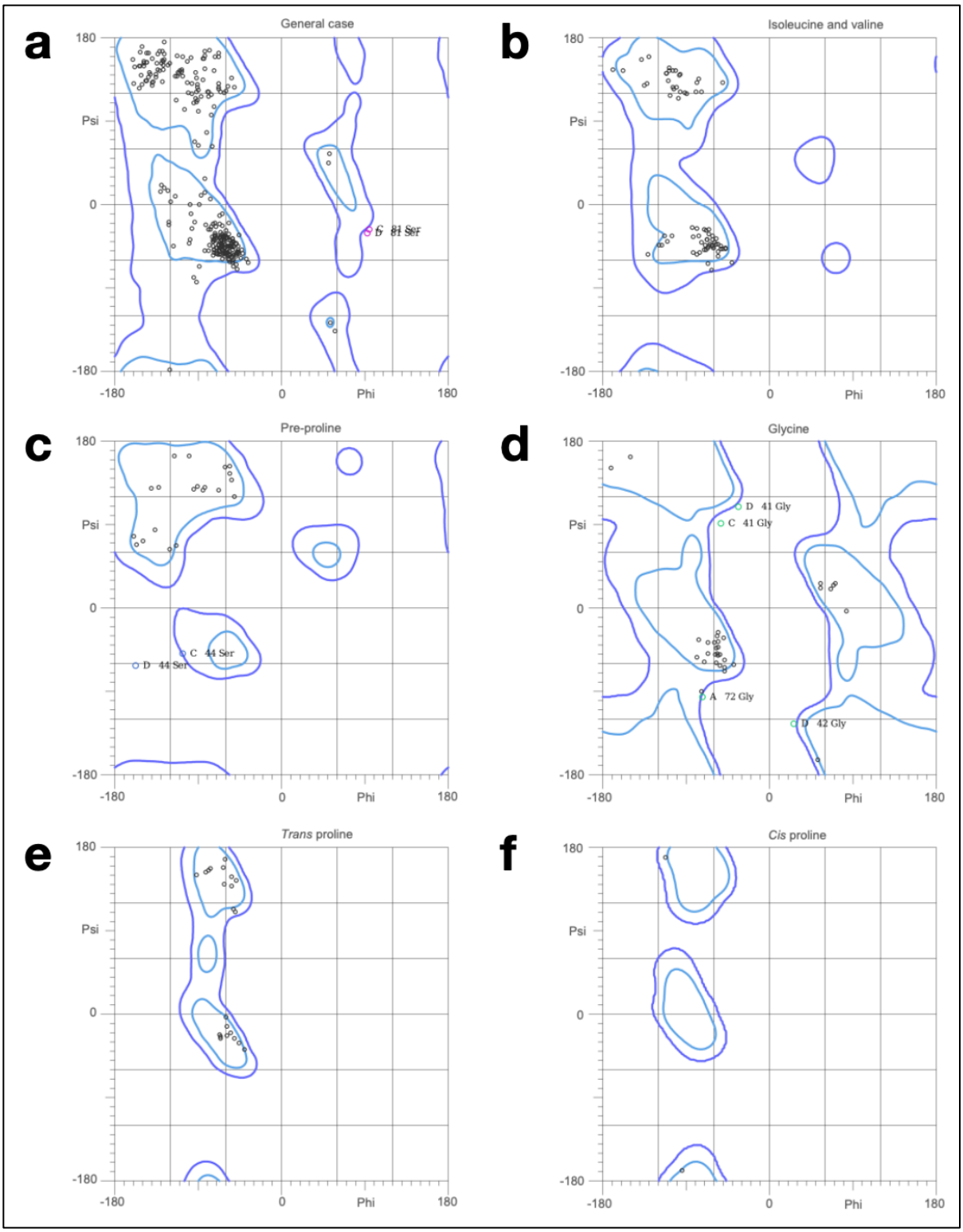


**Figure 10:** Ramachandran plots of the proposed structure. (**a**) General plot. (**b**) Isoleucine and valine plot. (**c**) Pre-proline plot. (**d**) Glycine plot. (**e**) Trans proline plot. (**f**) Cis proline plot.

**Table 2:** Data collection statistics.

| **Data collection** | |
|---|---|
| Space group | $P4_1$ |
| *Cell dimensions* | |
| *a*, *b*, *c* (Å) | 87.12, 87.12, 145.87 |
| $\alpha, \beta, \gamma$ (°) | 90, 90, 90 |
| Resolution (Å)[a] | 33.3-3.11 (3.2-3.11) |
| $R_{merge}$[a] | 1.234 (4.094) |
| R-pim[a] | 0.2104 (0.6708) |
| Mn $I / \sigma I$[a] | 8.13 (1.31) |
| CC(1/2)[a, b] | 85.1 (34.4) |
| Completeness (%)[a] | 99.76 (100.00) |

[a] Data from experiments resulting from a close collaboration with Dr. McIlwain, who has permitted me to include in this thesis some of the data he collected and analyzed.

[b] Statistics for the highest-resolution shell are shown in parentheses, r.m.s., root-mean-square.

**Table 3:** Crystallography table of statistics comparing the model before and after manual refinement

| | **Before** | **After** |
|---|---|---|
| $R_{work}/R_{free}$ | 24.2/26.66 | 24.4/26.55 |
| Ramachandran favored | 396 | 402 |
| Ramachandran outliers | 7 | 8 |
| Clashscore | 10.81 | 11.68 |
| R.m.s. deviations | | |
| Bond lengths (Å) | 0.0091 | 0.0094 |
| Bond angles (°) | 1.7543 | 1.6871 |

Other important metrics to examine are the $R_{work}$ and $R_{free}$ values. These values can be used to examine any biases that may negatively affect the structure. An $R_{free}$ value that is 3-5% higher than the $R_{work}$ value is usually preferred. According to **Table 3**, the $R_{free}$ value was 2.46%

higher than the $R_{work}$. After refinement, the difference decreased to 2.15%. This change may be due to bias while fitting residues into the electron density.

**Table 4:** Crystallography table of statistics comparing my proposed model with the published model (pdb:5A43)

| | **Proposed model** | **Published model** |
|---|---|---|
| Space group | $P4_1$ | |
| Resolution (Å) | 87.12-2.71 | 24.2-2.6 |
| No. reflections | 41164 | 34593 |
| $R_{work}/R_{free}$ | 24.4/26.55 | 22.4/26.4 |
| Ramachandran favored | 402 | 92.6 |
| Ramachandran outliers | 8 | 2.53 |
| Clashscore | 11.68 | |
| R.m.s. deviations | | |
| Bond lengths (Å) | 0.0094 | 0.009 |
| Bond angles (°) | 1.6871 | 1.5 |

When comparing the proposed model to the published model (pdb:5A43) in **Table 4**, the published model has a higher resolution. In addition, the published model has a larger $R_{free}$ value, which is about 4% higher than $R_{work}$. This suggests that the proposed model may have been more biased than the published model. Lastly, the published model has fewer Ramachandran outliers, but less Ramachandran favored. This tradeoff indicates that there are some drawbacks to both the published and proposed models. Therefore, further refinement of the proposed model is needed.

**Analysis of anion selectivity**

The factors contributing to the Fluc channel's specificity for $F^-$ over $Cl^-$ are still poorly understood. The planar lipid bilayer experiments below attempt to gauge the extent of anion selectivity.

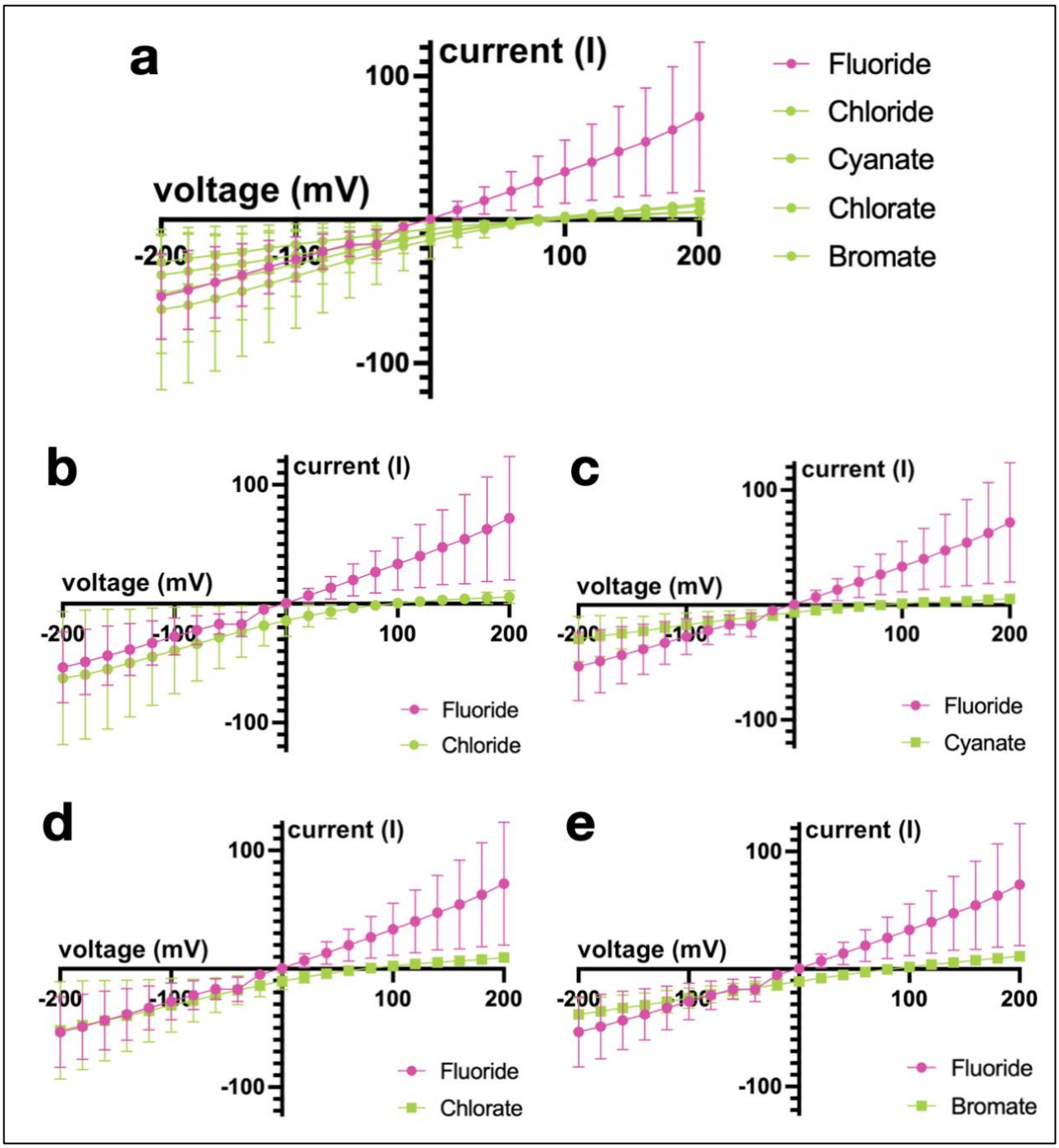


**Figure 11:** Reversal potentials of $F^-$ and anions tested are shown as the mean and SEM (standard error of mean) of measurements from independent bilayers. For every experiment, the fluoride buffer (290 mM KF and 10 mM NaF) was added to the cis chamber, while the buffer of the anion (290 mM KX and 10 mM NaX) tested was added to the trans chamber. All graphs show the same $F^-$ reversal potential (N=3 independent bilayers), which is expected to cross the x-axis at the origin of the graph. The $F^-$ reversal potential is shown in red, while all other reversal

potentials are shown in green. (**a**) Reversal potential of $F^-$ compared to the other anions tested. (**b-e**) Data dispersed from graph **a**. (**b**) Reversal potential of chloride (N=3 independent bilayers). (**c**) Reversal potential of cyanate (N=3 independent bilayers). (**d**) Reversal potential of chlorate (N=2 independent bilayers). (**e**) Reversal potential of bromate (N=3 independent bilayers).

**Table 5:** Reversal potential[a] of each anion

| Anion | Reversal potential (mV) |
|---|---|
| Fluoride ($F^-$) | −1.95 ± 6.25 |
| Chloride ($Cl^-$) | 95.54 ± 7.52 |
| Cyanate ($OCN^-$) | 81.95 ± 0.11 |
| Chlorate ($ClO_3^-$) | 74.41 ± 5.35 |
| Bromate ($BrO_3^-$) | 82.95 ± 8.61 |

[a] Mean and SEM of measurements from independent bilayers.

The reversal potential is the calculated membrane potential at which there is no net current flow through Fluc-Ec2. If the reversal potential is greater than the holding voltage, net current flow is inward, vice versa. As shown in **Figure 11** and **Table 5**, the $F^-$ reversal potential was found to be close to 0 mV, as expected. This result confirms that $F^-$ ions are highly permeable in Fluc channels. Surprisingly, the results suggest that all four anions tested are also permeable. Chlorate appears to be most permeable, followed by cyanate, bromate, and chloride.

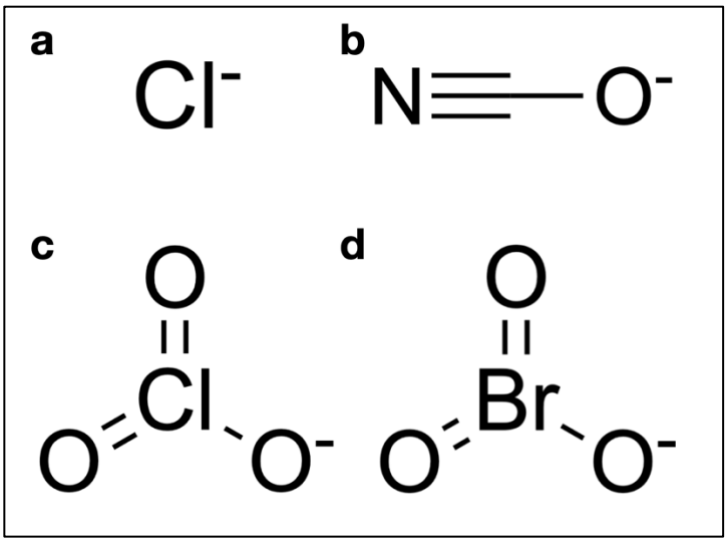


**Figure 12:** Structural formulas of the anions tested. (**a**) Chloride. (**b**) Cyanate. (**c**) Chlorate. (**d**) Bromate.

After closer examination of the structural formulas of each anion, as shown in **Figure 12**, chlorate, cyanate, and bromate may be more permeable than chloride due to the oxygen(s) present in their structures. The oxygen atom(s) found in the structures have lone pairs of electrons that make these anions excellent hydrogen bond acceptor candidates, which may be responsive to the hydrogen bond donors found in the polar track described in **Figure 7** and **Figure 8**. Due to the importance of this polar track, hydrogen bonding may play a role in how permeable each ion is. In addition, the higher permeability of chlorate compared to the other anions may be explained by the electronegativity of the chlorine atom. Compared to nitrogen in cyanate and bromide in bromate, chlorine is more electronegative. Since stronger hydrogen bonding is correlated to greater electronegativity of the hydrogen bond acceptor, chlorate may act as a better hydrogen bond acceptor. These factors may explain why chlorate appears to be more permeable than the other anions.

For these experiments, our initial assumption was that Fluc channels comprise a bionic system with only two permeant ions, $F^-$ and, potentially, the other ion tested. Given this assumption, the Nernst equation (**Equation 2**) was used to calculate the relative permeability of each anion.

$$E_{rev} = \frac{RT}{F} \times \ln\left(\frac{P_{F^-}}{P_{X^-}}\right)$$

**Equation 2:** Nernst equation for a two-ion system. $E_{rev}$ represents the reversal potential, which is calculated in units of volts. $R$ represents the universal gas constant, $8.314\ V \times C \times mol^{-1} \times K^{-1}$. $T$ represents temperature in kelvin, which was estimated to be $298\ K$ (room temperature, 25°C) during experiments. $F$ represents the Faraday constant, $96{,}485\ C \times mol^{-1}$. $P_{F^-}$ and $P_{X^-}$ represent the permeability of fluoride and the tested anion, respectively. The permeability value is unitless.

For **Calculation 1**, $P_{F^-}$ was arbitrarily set to equal 1.

$$\frac{RT}{F} = \frac{8.314\ V \times C}{mol \times K} \times 298\ K \times \frac{mol}{96{,}485\ C} = 0.0257\ V = 25.7\ mV$$

$$E_{rev} = 74.4\ mV = \frac{RT}{F} \times \ln\left(\frac{P_{F^-}}{P_{ClO_3^-}}\right) = 25.7\ mV \times \ln\left(\frac{1}{P_{ClO_4^-}}\right)$$

$$2.89 = \ln\left(\frac{1}{P_{ClO_3^-}}\right)$$

$$P_{ClO_3^-} = 0.055, \qquad \frac{P_{F^-}}{P_{ClO_3^-}} = 18.08$$

**Calculation 1:** Relative permeability of $ClO_3^-$, two-ion system.

**Calculation 1** was repeated for each anion in **Table 6**.

**Table 6:** Relative permeability of each anion, two-ion system

| **Anion, $X^-$** | **$\ln\left(\frac{P_{F^-}}{P_{X^-}}\right)$** | **Relative permeability of anion, $X^-$** | **$\frac{P_{F^-}}{P_{X^-}}$** |
|---|---|---|---|
| Chloride ($Cl^-$) | 3.72 | 0.024 | 41.16 |
| Cyanate ($OCN^-$) | 3.19 | 0.041 | 24.26 |
| Chlorate ($ClO_3^-$) | 2.89 | 0.055 | 18.08 |
| Bromate ($BrO_3^-$) | 3.23 | 0.040 | 25.22 |

According to **Table 6**, chlorate appears to be more than twice as permeable as chloride, while the relative permeabilities of cyanate and bromate are very similar. The two-ion system described above, however, does not consider the possibility of sodium ion permeation.

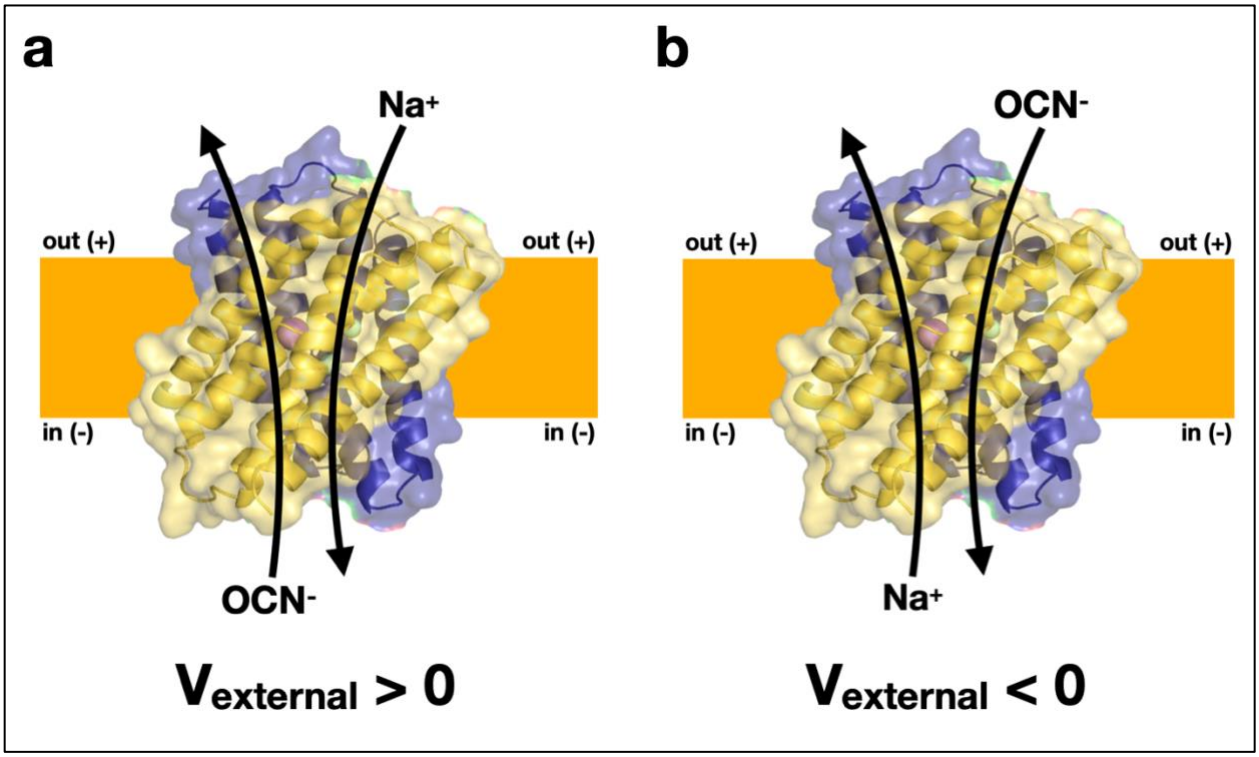


**Figure 13:** Direction of ion movement in different scenarios. Sodium, a cation, and cyanate, one of the anions tested, are shown. The yellow rectangle denotes the approximate membrane boundaries with typical membrane polarization indicated with plus and minus symbols. (**a**) When a positive voltage is applied to the system, cations flow inwards and anions flow outwards. (**b**) When a negative voltage is applied to the system, cations flow outwards and anions flow inwards.

As described in **Figure 13**, inward sodium movement is indistinguishable from outward cyanate movement. Therefore, it is important to consider that sodium may also be permeable. In this case, the Nernst potential is given by **Equation 3**.

$$E_{rev} = \frac{RT}{F} \times \ln\left(\frac{[F^-]P_{F^-} + [Na^+]P_{Na^+}}{[X^-]P_{X^-} + [Na^+]P_{Na^+}}\right)$$

**Equation 3:** Nernst equation for a three-ion system. $[F^-]$, $[Na^+]$, and $[X^-]$ represent the molar concentration of fluoride, sodium, and the tested anion, respectively. The sodium ion concentration, $[Na^+]$, is the same on both sides of the bilayer. $P_{Na^+}$ represents the permeability of sodium.

For **Calculation 2**, $P_{F^-}$ was arbitrarily set to equal 1. Because it is impossible to solve for all variables presented in **Equation 3**, the permeability of the anion, $P_{ClO_3^-}$, in **Calculation 2** was set to zero in order to set a limit on the maximum possible $Na^+$ permeation. Therefore, $P_{Na^+}$ is being solved for in **Calculation 2**.

$$E_{rev} = 74.41\ mV = \frac{RT}{F} \times \ln\left(\frac{[F^-]P_{F^-} + [Na^+]P_{Na^+}}{[ClO_3^-]P_{ClO_3^-} + [Na^+]P_{Na^+}}\right)$$

$$74.41\ mV = 25.7\ mV \times \ln\left(\frac{(0.3)(1) + (0.01)P_{Na^+}}{(0.3)(0) + (0.01)P_{Na^+}}\right)$$

$$18.08 = \frac{(0.3) + (0.01)P_{Na^+}}{(0.01)P_{Na^+}}$$

$$18.08[(0.01)P_{Na^+}] = 0.3 + (0.01)P_{Na^+}$$

$$(0.18)P_{Na^+} = 0.3 + (0.01)P_{Na^+}$$

$$(0.17)P_{Na^+} = 0.3$$

$$P_{Na^+} = 1.76, \qquad \frac{P_{F^-}}{P_{Na^+}} = 0.57$$

**Calculation 2:** Relative permeability of $Na^+$, three-ion system.

**Calculation 2** was repeated for each anion in **Table 7**.

**Table 7:** Relative permeability of sodium, three-ion system

| **Anion, $X^-$** | **Relative permeability of sodium** | $\frac{P_{F^-}}{P_{Na^+}}$ |
|---|---|---|
| Chloride ($Cl^-$) | 0.75 | 1.34 |
| Cyanate ($OCN^-$) | 1.29 | 0.78 |
| Chlorate ($ClO_3^-$) | 1.76 | 0.57 |
| Bromate ($BrO_3^-$) | 1.23 | 0.81 |

If the current reversal we observe is due to $Na^+$ rather than anion $X^-$, this would indicate that $Na^+$ is more permeable than $F^-$, as indicated in **Table 7**. According to experiments from Stockbridge et al. (2013), this does not seem reasonable. A slightly leaky bilayer may explain this inconsistency.

**Strength and validity of anion selectivity experiments**

As described in **Equation 3** and **Table 7**, the results presented in **Figure 11** and **Table 5** fail to consider $Na^+$ ion permeation. Therefore, a bromate gradient experiment was conducted to examine this possibility.

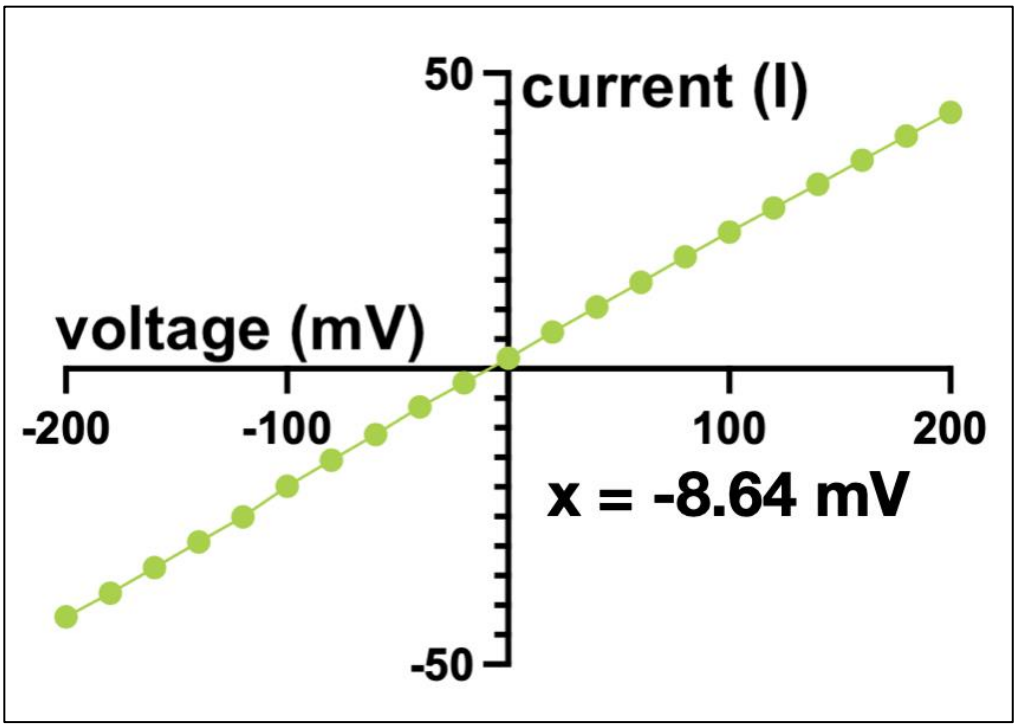


**Figure 14:** The reversal potential found in the bromate gradient experiment (N=1). One buffer (290 mM $KBrO_3$ and 10 mM $NaBrO_3$) was added to the cis chamber, while the other buffer (20 mM $KBrO_3$ and 10 $NaBrO_3$) was added to the trans chamber.

The reversal potential found in **Figure 14** crosses the x-axis near the origin. Because there is no $Na^+$ gradient present in this experiment, it would be expected to see a bromate reversal potential similar to the one in **Table 5** if bromate is permeable. However, this is not the case. Despite no $Na^+$ gradient, it appears that $Na^+$ is permeable and bromate is, in fact, not permeable. Therefore, this result suggests that the data presented in **Figure 11** and **Table 5** are sodium-dependent. As a result, none of the anions (chlorate, cyanate, bromate, and chloride) appear to be permeable.

This finding is surprising because experiments from Stockbridge et al. (2013) found that there was no $Na^+$ permeation when testing conditions were 300 mM NaF (cis chamber) and 30 mM NaF (trans chamber). These findings combined with the results presented in this thesis suggest that $Na^+$ permeation may be only present in the absence of $F^-$. In other words, when $F^-$ is present, it may be outcompeting $Na^+$. Furthermore, this argument is strengthened by the fact that $Na^+$ currents are only observed from the side of the bilayer where $F^-$ is absent. The structure of the channel also implies that the $Na^+$ structural element, which is essential for proper Fluc

conducting conformation, may play a role in this scenario (McIlwain et al., 2020). Though the $Na^+$ binds to a site formed by the cross of the two TM3 helices, it may contribute to the $Na^+$ currents observed in the results.

# Discussion

The model of the X-ray crystal structure proposed in this thesis provides insight into various residues and sequences of the channel that are important for its function. The highly conserved Arg19 and Asn41 residues and TGFXGGLTTFSTFSXE and polar track regions reveal vital structural details that allow the channel to function. Though some structural metrics can be improved in the proposed structure, the structural improvement observed after manual refinement suggests that the proposed structure is more accurate and refined. Future work should be done to further refine the proposed model. Emphasis should be placed on how bias may negatively affect the structural integrity of the model.

Preliminary anion selectivity assays suggested that chlorate, cyanate, bromate, and chloride are all permeable through the channel. It was suggested that the higher permeability is correlated with electronegativity and hydrogen bond accepting strength. However, the methodology of these experiments failed to recognize the possibility of sodium ion permeability. A subsequent assay revealed that the three-ion system is a more appropriate model to use. In fact, this experiment suggested that the previously thought polyatomic anion permeability is sodium ion-dependent. Although the anion specificity mechanism of Fluc channels is still largely unknown, these experiments contribute to the existing knowledge about these channels. Previous studies have examined the effects of various mutations to conserved regions of the channel, however, additional studies can be conducted in the future to hone the mechanistic features of anion selectivity.

**A note on science communication**

Over the past several years, science misinformation has rapidly spread throughout America, oftentimes fueled by social media, elected officials, and conspiracy theorists (Wang et al., 2019). All Americans — including the youth — are struggling to decipher real facts from fabricated lies (Wineburg & McGrew, 2016). To put it simply, Americans have been let down by institutions that should have cared more.

Thus, developing better methods of science communication is vital. Over this past semester, I have had the opportunity to study ceramics with Professor Susan Crowell. I was inspired to enroll in her course after seeing Hidden Worlds: The Universe of Pollen Revealed in

Large-scale Ceramic Sculptures, Prof. Crowell's exhibition of ceramic pollen sculptures. In collaboration with scientists at the University, she studied electron microscope images of pollen. Although Prof. Crowell may not be traditionally thought of as a scientist, her artwork shed light on the plight of bees (*Anthophila*), which are one of many species negatively affected by climate change (Soroye et al., 2020).

Inspired by Prof. Crowell's work, I will create a ceramic sculpture of the Fluc-Ec2 crystal structure that I solved. My goal is to highlight the beauty of Fluc channels through an examination of the intricacies of nature. The piece will be available for viewing on my website in late April 2022 (Ruprecht, 2022).

# References


Adamek, E., Pawłowska-Góral, K., & Bober, K. (2005). In vitro and in vivo effects of fluoride ions on enzyme activity. Annales Academiae Medicae Stetinensis,

Altschul, S. F., Gish, W., Miller, W., Myers, E. W., & Lipman, D. J. (1990). Basic local alignment search tool. *Journal of molecular biology*, *215*(3), 403-410.

Baker, J. L., Sudarsan, N., Weinberg, Z., Roth, A., Stockbridge, R. B., & Breaker, R. R. (2012). Widespread genetic switches and toxicity resistance proteins for fluoride. *Science*, *335*(6065), 233-235.

Barbier, O., Arreola-Mendoza, L., & Del Razo, L. M. (2010). Molecular mechanisms of fluoride toxicity. *Chemico-biological interactions*, *188*(2), 319-333.

Brammer, A. E., Stockbridge, R. B., & Miller, C. (2014). F−/Cl− selectivity in CLCF-type F−/H+ antiporters. *Journal of General Physiology*, *144*(2), 129-136.

Breaker, R. (2012). New insight on the response of bacteria to fluoride. *Caries research*, *46*(1), 78-81.

Breaker, R. R. (2012). Riboswitches and the RNA world. *Cold Spring Harbor perspectives in biology*, *4*(2), a003566.

Emsley, P., Lohkamp, B., Scott, W. G., & Cowtan, K. (2010). Features and development of Coot. *Acta Crystallographica Section D: Biological Crystallography*, *66*(4), 486-501.

Feng, L., Campbell, E. B., & MacKinnon, R. (2012). Molecular mechanism of proton transport in CLC Cl-/H+ exchange transporters. *Proceedings of the National Academy of Sciences*, *109*(29), 11699-11704.

Forrest, L. R., Krämer, R., & Ziegler, C. (2011). The structural basis of secondary active transport mechanisms. *Biochimica et Biophysica Acta (BBA)-Bioenergetics*, *1807*(2), 167-188.

Gouy, M., Guindon, S., & Gascuel, O. (2010). SeaView version 4: a multiplatform graphical user interface for sequence alignment and phylogenetic tree building. *Molecular biology and evolution*, *27*(2), 221-224.

Humphries, J., Xiong, L., Liu, J., Prindle, A., Yuan, F., Arjes, H. A., Tsimring, L., & Süel, G. M. (2017). Species-independent attraction to biofilms through electrical signaling. *Cell*, *168*(1-2), 200-209. e212.

Jagtap, S., Yenkie, M. K., Labhsetwar, N., & Rayalu, S. (2012). Fluoride in drinking water and defluoridation of water. *Chemical reviews*, *112*(4), 2454-2466.

Ji, C., Stockbridge, R. B., & Miller, C. (2014). Bacterial fluoride resistance, Fluc channels, and the weak acid accumulation effect. *Journal of General Physiology*, *144*(3), 257-261.

Last, N. B., Kolmakova-Partensky, L., Shane, T., & Miller, C. (2016). Mechanistic signs of double-barreled structure in a fluoride ion channel. *Elife*, *5*, e18767.

Last, N. B., & Miller, C. (2015). Functional monomerization of a ClC-type fluoride transporter. *Journal of molecular biology*, *427*(22), 3607-3612.

Last, N. B., Stockbridge, R. B., Wilson, A. E., Shane, T., Kolmakova-Partensky, L., Koide, A., Koide, S., & Miller, C. (2018). A CLC-type F-/H+ antiporter in ion-swapped conformations. *Nature structural & molecular biology*, *25*(7), 601-606.

Last, N. B., Sun, S., Pham, M. C., & Miller, C. (2017). Molecular determinants of permeation in a fluoride-specific ion channel. *Elife*, *6*, e31259.

Lebioda, L., Stec, B., Brewer, J. M., & Tykarska, E. (1991). Inhibition of enolase: the crystal structures of enolase-calcium (2+)-2-phosphoglycerate and enolase-zinc (2+)-phosphoglycolate complexes at 2.2-. ANG. resolution. *Biochemistry*, *30*(11), 2823-2827.

Lebioda, L., Zhang, E., Lewinski, K., & Brewer, J. M. (1993). Fluoride inhibition of yeast enolase: Crystal structure of the enolase–Mg2+–F−–Pi complex at 2.6 Å resolution. *Proteins: Structure, Function, and Bioinformatics*, *16*(3), 219-225.

Li, L. (2003). The biochemistry and physiology of metallic fluoride: action, mechanism, and implications. *Critical Reviews in Oral Biology & Medicine*, *14*(2), 100-114.

Li, S., Smith, K. D., Davis, J. H., Gordon, P. B., Breaker, R. R., & Strobel, S. A. (2013). Eukaryotic resistance to fluoride toxicity mediated by a widespread family of fluoride export proteins. *Proceedings of the National Academy of Sciences*, *110*(47), 19018-19023.

Macdonald, C. B., & Stockbridge, R. B. (2017). A topologically diverse family of fluoride channels. *Current opinion in structural biology*, *45*, 142-149.

McCoy, A. J., Grosse-Kunstleve, R. W., Adams, P. D., Winn, M. D., Storoni, L. C., & Read, R. J. (2007). Phaser crystallographic software. *Journal of applied crystallography*, *40*(4), 658-674.

McIlwain, B. C., Gundepudi, R., Koff, B. B., & Stockbridge, R. B. (2021). The fluoride permeation pathway and anion recognition in Fluc family fluoride channels. *Elife*, *10*, e69482.

McIlwain, B. C., Martin, K., Hayter, E. A., & Stockbridge, R. B. (2020). An interfacial sodium ion is an essential structural feature of Fluc family fluoride channels. *Journal of molecular biology*, *432*(4), 1098-1108.

McIlwain, B. C., Newstead, S., & Stockbridge, R. B. (2018). Cork-in-bottle occlusion of fluoride ion channels by crystallization chaperones. *Structure*, *26*(4), 635-639. e631.

McIlwain, B. C., Ruprecht, M. T., & Stockbridge, R. B. (2021). Membrane exporters of fluoride ion. *Annual review of biochemistry*, *90*, 559-579.

Miller, C., & Nguitragool, W. (2009). A provisional transport mechanism for a chloride channel-type Cl−/H+ exchanger. *Philosophical Transactions of the Royal Society B: Biological Sciences*, *364*(1514), 175-180.

Murshudov, G. N., Skubák, P., Lebedev, A. A., Pannu, N. S., Steiner, R. A., Nicholls, R. A., Winn, M. D., Long, F., & Vagin, A. A. (2011). REFMAC5 for the refinement of macromolecular crystal structures. *Acta Crystallographica Section D: Biological Crystallography*, *67*(4), 355-367.

Picollo, A., Malvezzi, M., Houtman, J. C., & Accardi, A. (2009). Basis of substrate binding and conservation of selectivity in the CLC family of channels and transporters. *Nature structural & molecular biology*, *16*(12), 1294-1301.

Potterton, E., Briggs, P., Turkenburg, M., & Dodson, E. (2003). A graphical user interface to the CCP4 program suite. *Acta Crystallographica Section D: Biological Crystallography*, *59*(7), 1131-1137.

Ren, A., Rajashankar, K. R., & Patel, D. J. (2012). Fluoride ion encapsulation by Mg2+ ions and phosphates in a fluoride riboswitch. *Nature*, *486*(7401), 85-89.

Ruprecht, M. T. (2022). *Ceramics portfolio*. http://fluc.michalruprecht.com

Schrodinger, L. (2010). The PyMOL molecular graphics system. *Version*, *1*(5), 0.

Smith, K. D., Gordon, P. B., Rivetta, A., Allen, K. E., Berbasova, T., Slayman, C., & Strobel, S. A. (2015). Yeast Fex1p is a constitutively expressed fluoride channel with functional

asymmetry of its two homologous domains. *Journal of Biological Chemistry*, *290*(32), 19874-19887.
Soroye, P., Newbold, T., & Kerr, J. (2020). Climate change contributes to widespread declines among bumble bees across continents. *Science*, *367*(6478), 685-688.
Stockbridge, R. B., Koide, A., Miller, C., & Koide, S. (2014). Proof of dual-topology architecture of Fluc F− channels with monobody blockers. *Nature communications*, *5*(1), 1-5.
Stockbridge, R. B., Kolmakova-Partensky, L., Shane, T., Koide, A., Koide, S., Miller, C., & Newstead, S. (2015). Crystal structures of a double-barrelled fluoride ion channel. *Nature*, *525*(7570), 548-551.
Stockbridge, R. B., Lim, H.-H., Otten, R., Williams, C., Shane, T., Weinberg, Z., & Miller, C. (2012). Fluoride resistance and transport by riboswitch-controlled CLC antiporters. *Proceedings of the National Academy of Sciences*, *109*(38), 15289-15294.
Stockbridge, R. B., Robertson, J. L., Kolmakova-Partensky, L., & Miller, C. (2013). A family of fluoride-specific ion channels with dual-topology architecture. *Elife*, *2*, e01084.
Stockbridge, R. B., & Tsai, M.-F. (2015). Lipid reconstitution and recording of recombinant ion channels. In *Methods in enzymology* (Vol. 556, pp. 385-404). Elsevier.
Turman, D. L., Nathanson, J. T., Stockbridge, R. B., Street, T. O., & Miller, C. (2015). Two-sided block of a dual-topology F− channel. *Proceedings of the National Academy of Sciences*, *112*(18), 5697-5701.
Turman, D. L., & Stockbridge, R. B. (2017). Mechanism of single-and double-sided inhibition of dual topology fluoride channels by synthetic monobodies. *Journal of General Physiology*, *149*(4), 511-522.
Wang, Y., McKee, M., Torbica, A., & Stuckler, D. (2019). Systematic literature review on the spread of health-related misinformation on social media. *Social science & medicine*, *240*, 112552.
Weinstein, L. H., & Davison, A. (2004). *Fluorides in the environment: effects on plants and animals*. Cabi.
Williams, C. J., Headd, J. J., Moriarty, N. W., Prisant, M. G., Videau, L. L., Deis, L. N., Verma, V., Keedy, D. A., Hintze, B. J., & Chen, V. B. (2018). MolProbity: More and better reference data for improved all-atom structure validation. *Protein Science*, *27*(1), 293-315.
Wineburg, S., & McGrew, S. (2016). Evaluating information: The cornerstone of civic online reasoning.
Winn, M. D., Ballard, C. C., Cowtan, K. D., Dodson, E. J., Emsley, P., Evans, P. R., Keegan, R. M., Krissinel, E. B., Leslie, A. G., & McCoy, A. (2011). Overview of the CCP4 suite and current developments. *Acta Crystallographica Section D: Biological Crystallography*, *67*(4), 235-242.